AGU ADVANCING EARTH AND SPACE SCIENCE

Geophysical Research Letters®

RESEARCH LETTER
10.1029/2021GL094418

Turbulence Analysis in Long-Range-Transported Saharan Dust Layers With Airborne Lidar

M. Gutleben[1,2] and S. Groß[1]

[1]Deutsches Zentrum für Luft- und Raumfahrt, Institut für Physik der Atmosphäre, Oberpfaffenhofen, Germany, [2]Meteorologisches Institut, Ludwig-Maximilians-Universität, Munich, Germany

M. Gutleben and S. Groß contributed equally to this work.

Key Points:

- First spectral analysis of airborne lidar data in long-range-transported Saharan dust layers
- Richardson numbers point toward mixing processes in Saharan dust layers
- Derived power spectra highlight established mesoscale turbulence cascade in dust layers

Correspondence to:
M. Gutleben,
manuel.gutleben@dlr.de

Citation:
Gutleben, M., & Groß, S. (2021). Turbulence analysis in long-range-transported Saharan dust layers with airborne lidar. *Geophysical Research Letters*, *48*, e2021GL094418. https://doi.org/10.1029/2021GL094418

Received 25 MAY 2021
Accepted 23 AUG 2021

Abstract In this study, turbulent properties of long-range-transported Saharan dust layers are investigated for the first time using airborne backscatter and water vapor lidar measurements. This is achieved via the utilization of spectral signal decomposition to the collected lidar data. Additionally, measurements by dropsondes are analyzed in detail. The presented measurements were conducted during the Next-Generation Aircraft Remote Sensing for Validation Studies II in boreal summer 2016 upstream Barbados. An analysis of two case studies shows that the derived mesoscale turbulence cascades inside the transported dust layers follow the predicted slopes for turbulence of −5/3. The turbulent nature of the Saharan air layers (SALs) is additionally indicated by small Richardson numbers, which are derived from data collected by launched dropsondes. These presented results also fortify the hypothesis that turbulence inside dust layers helps to keep large mineral dust particles aloft for a longer time, so that they can still be found after long-range transport.

Plain Language Summary Each year great amounts of Saharan mineral dust particles get transported westwards over the Atlantic Ocean in elevated dust layers. However, it is still not fully understood why dust particles of large diameters (tens of microns) can still be found in the Caribbean. According to Stokes theory, they would already be deposited at the beginning of their transport. In this study, for the first time, spectral signal decomposition is applied on airborne lidar measurements of long-range-transported Saharan dust layers. In this way, it is shown that turbulence inside the dust layers is well established. As a reason, large dust particles remain in the atmosphere for a longer time and can potentially be transported this far away from their source region.

1. Introduction

Earth's greatest source region of mineral dust aerosol is the Saharan desert and its arid surrounding landscapes. Approximately 50% of the global mineral dust aerosol load (400–2,200 $\mathrm{Tg}\,a^{-1}$) is estimated to be annually emitted in North Africa (Huneeus et al., 2011). Especially in the summer months, strong surface heating events over the Sahara cause pronounced thermal low-pressure systems which generate deep and well-mixed boundary layers of ∼6 km vertical extent (e.g., Messager et al., 2009). In this way, surface winds can mix dust particles up to great altitudes, where they get carried westwards embedded in the trade wind flow. As a reason, elevated layers of Saharan mineral dust are frequently advected over long distances toward the Caribbean and Central America (Moulin et al., 1997). Such layers are generally known as long-range-transported Saharan Air Layers (SALs, Prospero & Carlson, 1972; Carlson & Prospero, 1972).

Although the investigation of long-range-transported SALs has already been the focus during several extensive field campaigns (e.g., the Puerto Rico Dust Experiment [PRIDE; Reid, 2003], the Saharan Aerosol Long-Range Transport and Aerosol-Cloud-Interaction Experiment [SALTRACE; Weinzierl et al., 2017] or the Next-Generation Aircraft Remote Sensing for Validation Studies II [NARVAL-II; Stevens et al., 2019]), one important research questions still remains unanswered: Why are mineral dust particles of tens of microns diameter still found inside SALs after long-range-transport over the Atlantic Ocean? Measurements of particle size distributions in SALs have been performed near source regions (e.g., Weinzierl et al., 2011) as well as in regions before and after long-range SAL-transport in the vicinity of Cape Verde and the Caribbean (Maring, 2003; Weinzierl et al., 2017). No significant changes have been observed and large particles (10–30 μm) were still found inside SALs over the Caribbean. However, according to Stokes gravitational settling theory, they should have already been removed from the atmosphere several days before arriving

in the Caribbean (Bagnold, 1941). In addition to in situ observations, complementary lidar measurements were performed during the Saharan Mineral Dust Experiments SAMUM-I (Freudenthaler et al., 2009) and SAMUM-II (Groß et al., 2011) as well as the SALTRACE (Groß et al., 2015) project. Except for the expected decrease in SAL optical thickness, no significant differences in optical properties of SALs were observed. This was also the case for measurements conducted during NARVAL-II (Gutleben, Groß, & Wirth, 2019) which supports the hypothesis of an undisturbed dust transport. Moreover, observations of dust particle size distributions in the Caribbean show a nearly unchanged mean particle size compared to the distributions that are measured near source regions (e.g., Sunnu et al., 2008).

In recent years, several studies aimed at unraveling the processes behind decelerated dust sedimentation rates and soon two major mechanisms emerged to be potentially responsible, that is, SAL vertical mixing generated by radiative heating (Gasteiger et al., 2017; Gutleben, Groß, Wirth, et al., 2019; Gutleben et al., 2020) or electrostatic levitation of the dust particles (Nicoll et al., 2010; Renard et al., 2018). Studies that tried to explain the reduced fall speed of large dust particles via electrostatic levitation focused on investigations of relative dust particle polarities compared to the atmospheric electric fields. However, up to now, the electrostatic effect is not quantified for long-range particle transport inside SALs and further research is needed (van der Does et al., 2018). Gasteiger et al. (2017) used an integrated model and measurement approach to investigate particle settling processes during SAL advection. They conjectured that daytime convective mixing within the SAL could be the main driver for particle mixing and would allow dust particles with diameters larger than 20 μm to arrive in the Caribbean. However, radiative heating effects from dust particles alone could not explain vertical mixing inside the SALs.

Recently, airborne lidar measurements indicated enhanced water vapor mass mixing ratios in SAL-altitudes compared to the dry and dust-free surrounding troposphere (Gutleben, Groß, Wirth, et al., 2019). It was found that the shapes and magnitudes of the radiative heating profiles in regions influenced by long-range-transported SALs are mainly governed by water vapor absorption and emission and not by aerosol radiative effects (Gutleben et al., 2020). Associated water vapor radiative cooling with altitude can induce static instability, promote mixing processes and can help large dust particles to remain inside the dust layers during transport. Additionally, as a consequence of radiative cooling, the confining inversions at the top and the bottom of the SALs are maintained.

Up to now, turbulent and dynamic processes in and around long-range-transported SALs have never been investigated as such analyses usually require highly resolved in situ measurements of the wind components. However, previous studies have shown that spectral decomposition of lidar return signals can be utilized to remotely study the dynamics and turbulent features of cirrus clouds or propagating gravity waves (e.g., Demoz et al., 1998; Reichert et al., 2019; Wang & Sassen, 2008). Wang and Sassen (2006); Wang and Sassen (2008) for instance, analyzed the dynamical structure of cirrus mammatus and cirrus uncinus clouds by applying spectral methods on measurements from a ground-based backscatter lidar and a W-Band radar. They demonstrated that measured lidar-backscatter can be directly linked to the content of the cirrus itself, that is, to particle concentrations. Under additional assumption of Taylor's frozen turbulence hypothesis (Taylor, 1935), they spectrally analyzed fluctuations in measured backscatter coefficients. Their derived spectra of power spectral density (PSD) of the measured backscatter perturbations were interpreted as proxies for the distribution of turbulent kinetic energy (TKE) in the air mass and could thus be related to wave motions and turbulence.

Motivated by these findings, this study focuses for the first time on the investigation of dynamical and turbulent processes in regions affected by long-range-transported SALs by means of airborne lidar remote sensing, spectral signal decomposition and dropsonde measurements. Airborne backscatter and water vapor lidar measurements during NARVAL-II are analyzed with the goal to study variations in the backscattered signal using power spectra. In this way, mesoscale turbulent processes as well as the dynamics in a SAL-influenced atmosphere can be uncovered and studied. An extensive investigation of data collected by dropsondes complements the spectral analysis. This contributes to a better understanding of long-range dust transport.

The paper is structured as follows. Section 2 gives an overview of the used lidar instrument, the conducted field campaign as well as the utilized methods for the analysis of atmospheric turbulence. In Section 3, the

main findings of the analysis are presented by means of representative case studies. Results are summarized and conclusions from the performed analysis are drawn in Section 4.

2. Methods

2.1. The WALES Lidar Instrument

In this study, measurements of the airborne lidar system WALES (Water Vapor Lidar Experiment in Space; Wirth et al., 2009) are spectrally analyzed. WALES combines two lidar techniques that are well suited for aerosol and cloud remote sensing, that is, the water vapor differential absorption lidar (DIAL) technique and the depolarization-sensitive high spectral resolution lidar technique (HSRL; Esselborn et al., 2008). The DIAL module of WALES operates at four wavelengths in the 935 nm absorption band of water vapor and enables highly sensitive measurements of water vapor mass concentrations (r_m) that cover the whole extent of the troposphere. Needed narrow-band wavelength operation around the water vapor absorption band is guaranteed using injection-seeded optical parametrical oscillators (Mahnke et al., 2007) together with potassium titanyl phosphate acting as nonlinear material. In addition to the DIAL capability, depolarization sensitive HSRL measurements at 532 nm allow direct measurements of particle extinction coefficients, particle linear depolarization ratios $\delta_{p(532)}$ and the backscatter ratios $R_{532_{\|}}$ between the total and the molecular backscatter coefficients. The most important performance parameters and a detailed instrument description can be found in Wirth et al. (2009).

WALES measurements are temporally and spatially averaged for noise reduction. This results in horizontal resolutions of ~3 km for DIAL measurements and 0.2 km for HSRL measurements at typical aircraft speed. The vertical resolution amounts to 150 and 15 m, respectively. For DIAL measurements, uncertainties are estimated to be smaller than 5%, as pulses are repeated at the very high rate of 200 Hz (Kiemle et al., 2008). Measurement uncertainties of 5% for $R_{532_{\|}}$ and 10%–16% for $\delta_{p(532)}$ have to be considered as well.

2.2. The NARVAL-II Field Campaign With the HALO Research Aircraft

The main objective of the NARVAL-II research campaign was to explore subtropical atmospheric circulation patterns and to study the formation and evolution of clouds during boreal summer 2016. The summer months also mark the peak-season of transatlantic dust-transport to the Caribbean (Prospero & Lamb, 2003). As a result, it was possible to design research flights to regions covered by long-range-transported Saharan dust. This enabled an in-depth investigation of the SALs and their properties (Gutleben, Groß, Wirth, et al., 2019; Gutleben et al., 2020). During NARVAL-II the WALES instrument was operated in a downward-looking setup aboard HALO (High Altitude and Long Range research aircraft; Krautstrunk & Giez, 2012). HALO has a ceiling altitude of ~15 km and can cover distances of up to ~12,000 km. During the period of NARVAL-II in August 2016, HALO was based on the island of Barbados at the Grantley Adams International Airport (Stevens et al., 2019).

In this study, mesoscale turbulent structures in SALs and their environment are investigated on the basis of lidar data collected during the research flights on August 12 and 19, 2016 (RF3 and RF6). As dropsondes were launched at a high frequency during those flights, collected meteorological data complements the lidar-measurements. RF3 and RF6 were specifically designed to lead over a long-range-transported SALs over the North Atlantic Ocean where measured total column aerosol optical depths (AODs; Figure 1) took values around 0.3 (RF3) and >0.4 (RF6). As the flights also aimed for studying mesoscale tropospheric vertical motions using dropsondes (Bony & Stevens, 2019), flight tracks were designed to contain circular patterns.

2.3. Lidar- and Dropsonde-Based Turbulence Analysis

TKE is an important measure in fluid-dynamics and turbulence-analysis. It represents the part of kinetic energy in a flow, that is associated with eddies and waves. In classical physics, kinetic energy E_k is given by $E_k = \frac{mv^2}{2}$, with m being the mass and v being velocity. The subtraction of the mean velocity components from the velocity field in this equation yields the TKE - the portion of the energy per unit mass associated

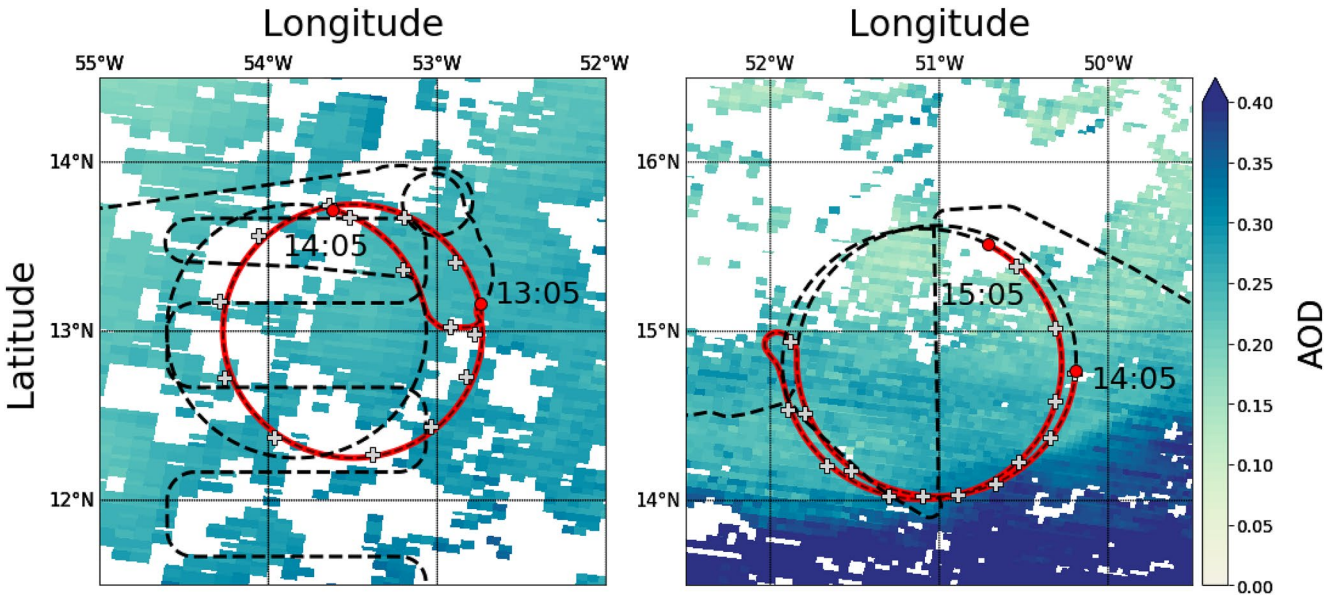

Figure 1. High altitude and long range research aircraft (HALO) flight tracks on August 12 (RF3, left) and 19, 2016 (RF6, right) on top of MODIS (Moderate Resolution Imaging Spectroradiometer) imagery of total column aerosol optical depth (AOD) taken aboard the Aqua satellite around 13:40 UTC. The blue lines indicate the flight segments used for the analysis. Red points indicate its start and end time-stamps and gray crosses mark the locations of the launched dropsondes.

only with the turbulent perturbations of the mean wind components ($\overline{u'^2}$, $\overline{v'^2}$, $\overline{w'^2}$). For an atmospheric flow, it can be expressed as follows,

$$\frac{\mathrm{TKE}}{m} = \frac{\overline{u'^2} + \overline{v'^2} + \overline{w'^2}}{2} = A + B + G + T - \epsilon. \tag{1}$$

Here, A is the advection of TKE by the mean wind, B is the buoyant production or loss of turbulence, G is the mechanical generation of turbulence by flow shear, T is the transport of TKE by the turbulence itself and ϵ is the dissipation of TKE. B can take positive or negative values. A and T just redistribute TKE and do not generate and destroy TKE. G is always greater or equal to zero and the dissipation ϵ is always negative. Hence, TKE always decreases toward zero.

In 1941, A. N. Kolmogorov derived a formula for the energy spectrum of turbulence in a quasi-isotropic flow (Kolmogorov, 1941). He stated that TKE is fed to the system in the form of large eddies. Smaller eddies then feed from the energy of larger eddies. Hence, a cascade of energy from large eddies to small eddies is induced. As a result, the turbulent energy spectrum $E(k)$ in the so-called inertial subrange (<1 km) follows a slope of $-5/3$ and is described by the equation:

$$E(k,\zeta) = \Phi k^{-5/3} \zeta^{2/3}. \tag{2}$$

Here, Φ is Kolmogorov's constant, ζ is the energy dissipation rate and k is the wavenumber. When a slope of $-5/3$ is extending to larger scales of up to several tens of kilometers, turbulent energy gets transferred, up-scaled and quasi-two-dimensional mesoscale eddies are formed (Lilly, 1983). Since the minimum horizontal resolution of the WALES lidar system is 200 m, these scales (1–100 km) are of particular interest in this study.

Another measure for atmospheric turbulence is the so-called Richardson number (Ri). It is the ratio of buoyant production and mechanical generation of turbulence by flow shear. Ri is defined as the ratio of the squared Brunt Väisälä frequency N^2 and G:

$$Ri = \frac{-B}{G} = \frac{N^2}{G} = \frac{\frac{g}{\Theta}\frac{\partial \Theta}{\partial z}}{\left(\frac{\partial u}{dz}\right)^2 + \left(\frac{\partial v}{dz}\right)^2}. \tag{3}$$

In this equation, g is the gravitational acceleration and Θ is potential temperature. The greater Ri, the lower the chance for turbulence to be generated. According to stability theory, Ri even has to be smaller than a critical value of 1/4 for the formation of turbulence (e.g., Turner, 1973). In this study, an analysis of Ri using dropsonde data additionally aims for resolving turbulent regions in the lidar profiles.

This study for the first time expounds a lidar-based analysis of atmospheric turbulence and dynamics in regions affected by long-range-transported Saharan dust layers. The backscattered power in a certain range interval of WALES lidar measurements can be interpreted to be a proxy for variations of aerosol and concentrations in the dust layer, as it is directly linked to variations of particle concentrations. In this way, turbulent eddies can be reconstructed from time series of backscatter and water vapor measurements and conclusions on the dynamics and the turbulence in desired atmospheric regions can be drawn.

Here, perturbations of $R_{532_{\|}}$ and r_m are spectrally decomposed to periodograms of PSD using the Lomb-Scargle-method, for unevenly spaced observations (Lomb, 1976; Scargle, 1982). Such spectral analyses of spatially resolved measurements are performed to detect dominant length scales in signal variability and, consequently, the distribution of energy as a function of eddy length. The derived spectral slopes of the power spectra correspond to the turbulent activities in these regions. To obtain the needed perturbations for calculations in the respective signals, the mean values of the time series are subtracted from the individual measurements according to Reynolds averaging:

$$\overline{R_{532}}' = R_{532} - \overline{R_{532}} \tag{4}$$

$$\overline{r_m}' = r_m - \overline{r_m} \tag{5}$$

Here, $\overline{R_{532}}$ and $\overline{r_m}$ represent the mean components of the backscatter and water vapor measurements and $\overline{R_{532}}'$ and $\overline{r_m}'$ are the respective fluctuating parts.

3. Results

To evaluate turbulent processes inside long-range-transported SALs and the subjacent marine boundary layer (MBL), two 1-h-lidar data sets (550 and 590 km length) collected in the framework of the NARVAL-II research flights RF3 and RF6 are analyzed. Figure 2 gives an overview of the measurement situations and the meteorological conditions derived from dropsondes during that flights (14 dropsondes each).

During both flights, measurements of $\delta_{p(532)}$ exhibit typical values for transported mineral dust of approximately 30%. In the course of RF6 a distinct SAL, which ranged from 2.7 to 4.0 km altitude and was well-separated from the MBL below (0.0–1.7 km), was observed. In contrast, the SAL observed during RF3 (1.2–4.2 km) was directly located on top of the MBL. $R_{532_{\|}}$ in both SALs were enhanced and ranged from 2 to 5. Measurements of r_m and equivalent potential temperature (Θ_e) highlight that the observed SALs came along with enhanced concentrations of water vapor ($\approx$4 g kg^{-1};$\Theta_e \approx 330\,K$) compared to the atmosphere below and above (see also Gutleben, Groß, Wirth, Emnde, & Mayer, 2019; Gutleben et al., 2020). During both flights, the SALs represented decoupled layers as wind speeds and directions differed from the ones in the surrounding regions. While wind speeds during RF3 were considerably higher in the SAL (20–25 kt [10.0–12.5 m s^{-1}]) than above and below, they were weaker in the SAL (5–10 kt [2.5–5.0 m s^{-1}]) than above and below during RF6. In addition, wind directions during RF6 differed (winds from north-west) from the ones in the MBL below (easterly winds). In both cases, the SAL was confined by inversions. During RF6 a total of three inversions could be detected in vertical measurements of temperature (T), Θ and Θ_e. One was located at the top of the MBL (1.7 km) and the other two confined the SAL at its top (4.0 km) and bottom (2.7 km). The bottom inversion of the SAL during RF3 merged with the trade wind inversion below. Hence, only two inversions were observed on August 12, 2016. Both SALs were observed to represent neutrally stratified layers (Θ and Θ_e are constant with height) and should have therefore been well mixed.

To spot turbulent regions in the observed vertical columns by dropsondes, squared Brunt-Väisälä frequencies, as well as derived wind shears and Richardson numbers are investigated in detail (Figure 3). Both observed scenes are characterized by small N^2 in SAL regions ($< 0.1 \cdot 10^{-4}\,s^{-2}$), an indicator for neutral stratification, the lack of buoyant stability and the potential for mixing. Relatively great values of N^2 restrict the

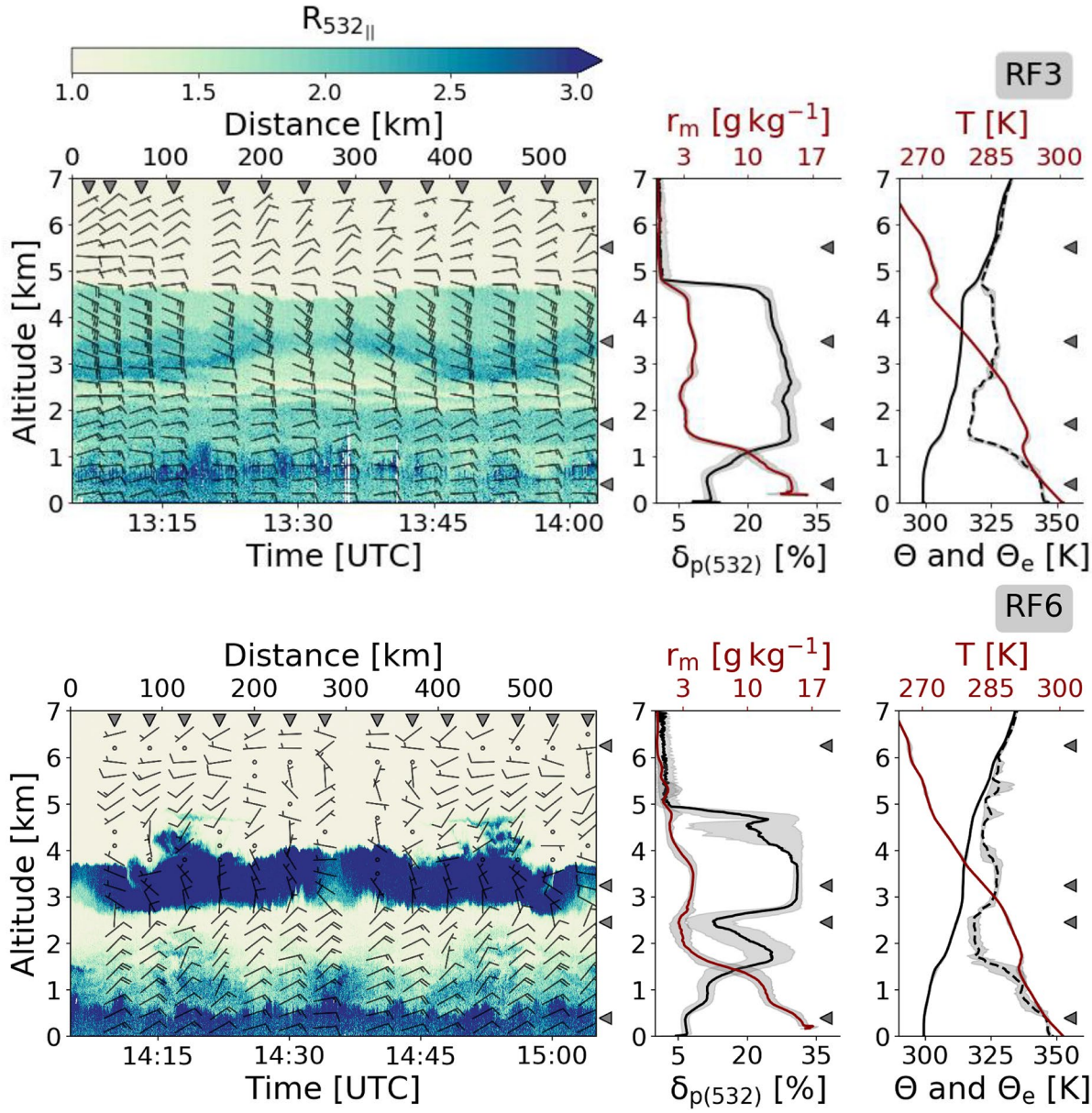

Figure 2. Left: Cross sections of measured lidar backscatter ratio at 532 nm ($R_{532||}$) over two long-range-transported Saharan air layers (SALs) observed on August 12 (RF3, top) and 19(RF6, bottom), 2016 upstream Barbados. Wind barbs indicate the measured horizontal wind speeds and directions measured by these sondes. Middle: Median profiles of particle linear depolarization ratio $\delta_{p(532)}$ (black) and water vapor mixing ratio r_m (red) for the measurement segments shown left. Right: Median profiles of temperature T (red), potential temperature Θ (black, solid) and equivalent potential temperature Θ_e (black, dashed) as measured by the sondes. Gray shadings in the middle and left panels indicate the respective interquantile ranges (0.25–0.75). Locations of dropped meteorological sondes as well as chosen altitudes for spectral signal decomposition are marked by gray triangles.

SALs at their top and their bottom ($> 0.5 \cdot 10^{-4}\, s^{-2}$). Those regions can be attributed to the two confining inversions which come along with great static stability. The same features are also observed in wind shear. Horizontal wind shear is smallest inside the observed SALs ($< 0.1 \cdot 10^{-4}\, s^{-2}$) and regions of great wind shear are found at their respective upper and the lower edges ($> 0.2 \cdot 10^{-4}\, s^{-2}$). This supports the hypothesis that the SALs represent decoupled atmospheric layers. N^2 to G, the Richardson number Ri, also shows smallest values inside the respective SALs. Greatest Ri is found at their top and bottom. These findings highlight that the SALs must be well mixed in their interior and that they are delimited at their top and bottom.To study the turbulent and dynamical processes in these SAL-influenced atmospheres in more detail, lidar power spectra for four different altitude ranges are calculated for both observed scenes, that is, inside the

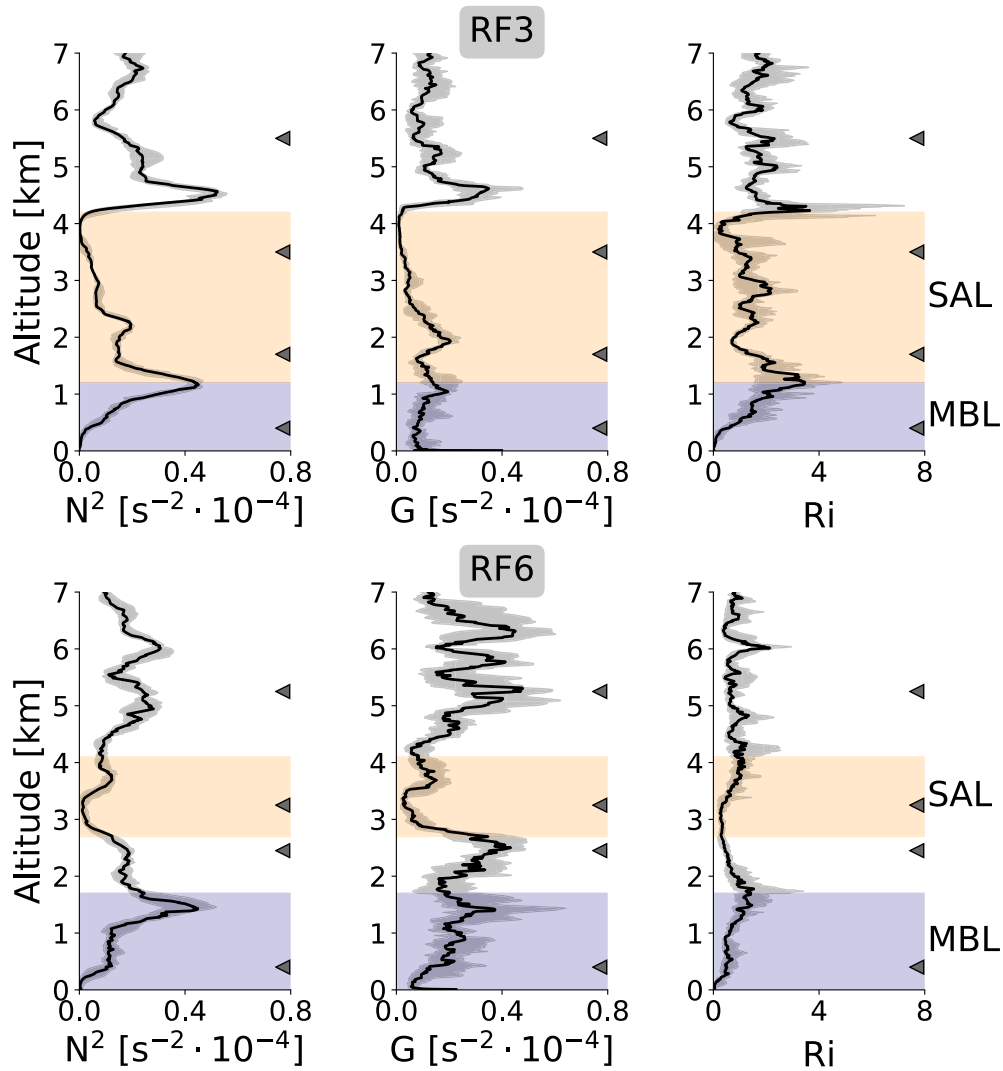

Figure 3. Derived median profiles of squared Brunt-Väisälä frequency (N^2), wind shear (G) and Richardson Number (Ri) from dropsondes launched during RF3 and RF6 on August 12 and 19, 2016 (see Figure 2). Gray shadings indicate interquantile ranges (0.25–0.75). Altitudes of the horizontal profiles used for signal decomposition are marked by gray triangles. Shadings indicate MBLs (light-blue) and SALs (light-brown).

MBL as well as inside, below and above the pronounced SALs (Figure 4). To double check the results of the turbulence cascade, power spectra for both, the higher resolved $R_{532_{\|}}$ as well as the lower resolved r_m are calculated. In the region from 10^{-2} Hz to 10^{-1} Hz (1–100 km wavelength), the derived PSD for $R_{532_{\|}}$ and r_m in SAL-altitudes (3.5 km [RF3] and 3.25 km [RF6]) approach the predicted slope of mesoscale turbulence, that is, −5/3. This indicates that the turbulent energy cascade inside the SAL is well established, that small-scale turbulence is transferred to the mesoscale and that the layer is well mixed. It also fits well to the observations of N^2, Ri, and Θ shown before. The PSD-spectra of $R_{532_{\|}}$ and r_m inside the SALs also indicate that wavelengths around 100 km carry the greatest energy. Power densities at scales of less than 1 km (0.1 Hz) cannot be resolved with this technique due to signal noise and the corresponding flattening of the slope in PSD. At 0.4 km and at 1.7 km (RF3), as well as 2.45 km (RF6), the slopes of $R_{532_{\|}}$-PSD are a little flatter and take values greater −5/3. Turbulent features are expected at these levels inside the MBL, however, it is an indication that the turbulence cascade is not fully developed. Boundary layer convection and its turbulent nature is most likely the reason for the signal fluctuations in the r_m and $R_{532_{\|}}$ time series. A not fully developed turbulence cascade at the lowermost levels is also found in the PSD-spectra for r_m for both flights.

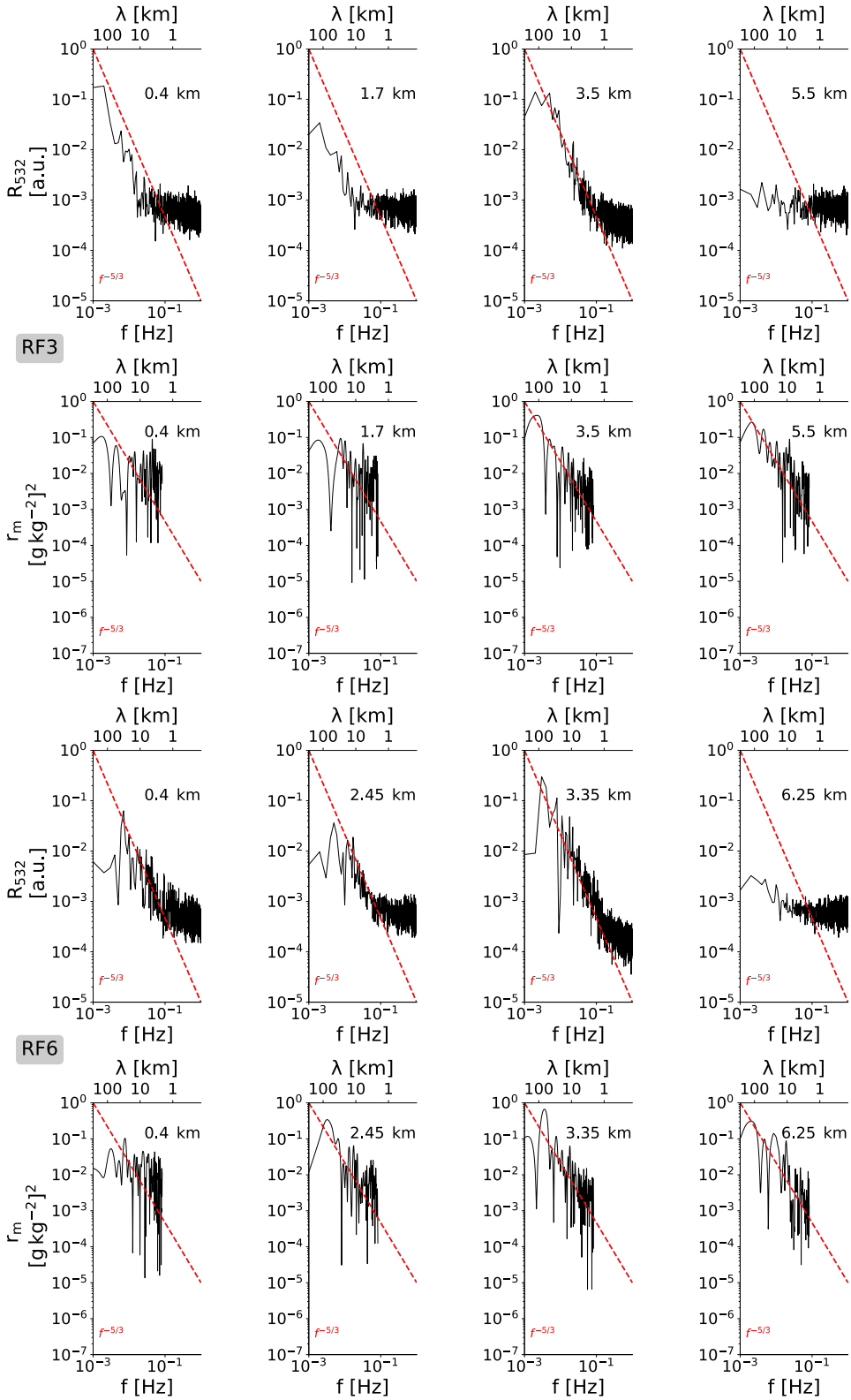

Figure 4. Calculated power spectral densities as a function of frequency f and wavelength λ of lidar backscatter ratio ($R_{532||}$, top) and water vapor mass mixing ratio (r_m, bottom) during RF3 (top eight panels) and RF6 (bottom eight panels) on August 12 and 19, 2016 at altitudes (z) indicated in Figure 2. In order to reduce noise, plotted power spectral densities of $R_{532||}$ correspond to averaged power densities of all spectra calculated in the interval $-75\ \text{m} < z < 75\ \text{m}$ (11 height intervals). The dashed lines indicate a slope of −5/3 (red) for comparison.

At highest levels in both scenes, above the SALs, the $R_{532||}$-spectra flatten and take values between $-1/6$ and -1. These spectra have to be interpreted very carefully, as the signal to noise ratio is small because of the lack of aerosol. Consequently, the derived slopes get flattened. However, Richardson numbers at these altitudes point toward the suppression of turbulence and great static stability. Slopes in the spectra of r_m are steeper since filaments of water vapor convective outflow at these altitudes were captured.

4. Summary and Conclusion

This study for the first time substantiated that spectral analyses of airborne lidar measurements can be employed to study mesoscale turbulence in regions affected by long-range-transported Saharan mineral dust layers. The analysis of two case studies shows that the SALs are vertically well mixed layers. An analysis of Brunt-Väisälä frequencies and Richardson numbers highlights that the SALs represent decoupled layers that are delimited by statically stable regions at their confining top and bottom. Inside the SALs, Richardson numbers take values around 0.25 - an indication that turbulence can potentially evolve. Gutleben, Groß, Wirth, et al. (2019); Gutleben et al. (2020) expected turbulence inside the SAL form derived differential vertical radiative heating rates. The results in this work, shows that mesoscale turbulent features inside the observed SALs are well established and endorse their presumption.

A spectral analysis of variations in the backscattered signals are interpreted as proxies for variations of TKE, as was already shown in previous studies concentrating on turbulent structures of cirrus clouds (Demoz et al., 1998; Wang & Sassen, 2006). Derived power spectra of both lidar backscatter ratio and water vapor mass mixing ratio indicate well-established turbulence cascades from larger toward smaller eddies inside SALs. The slopes of both spectra follow the predicted slopes of $-5/3$ for fully developed mesoscale turbulence. At altitudes below and above the SALs the slope of the cascade are flatter, thus pointing toward less developed dynamics and a clear separation from turbulent effects inside the SALs.

The observed findings also fortify the hypothesis that turbulence inside SALs helps to keep large mineral dust particles with diameters of several tens of microns aloft for a longer time and counteracts gravitational settling effects.

Conflict of Interest

The authors declare no conflicts of interest relevant to this study.

Data Availability Statement

The WALES lidar data used in this study were collected during the NARVAL-II (Next-Generation Aircraft Remote Sensing for Validation Studies II) and are published and available in the HALO database (https://halo-db.pa.op.dlr.de/mission/92; German Aerospace Center, 2016). The dropsonde data used in this study are published and described by Konow et al. (2018).

Acknowledgments
NARVAL-II was funded with the support of the Max Planck Society, the German Research Foundation (DFG Priority Program: HALO-SSP 1294) and DLR. The authors would like to thank the staff members of the German Aerospace Center (DLR) HALO aircraft from DLR Flight Experiments for preparing and performing the measurement flights. Open access funding enabled and organized by Projekt DEAL.

References

Bagnold, R. A. (1941). *The physics of blown sand and desert dunes*. London: Methuen.

Bony, S., & Stevens, B. (2019). Measuring area-averaged vertical motions with dropsondes. *Journal of the Atmospheric Sciences*, *76*(3), 767–783. https://doi.org/10.1175/jas-d-18-0141.1

Carlson, T. N., & Prospero, J. M. (1972). The large-scale movement of Saharan air outbreaks over the Northern Equatorial Atlantic. *Journal of Applied Meteorology*, *11*, 283–297. https://doi.org/10.1175/1520-0450(1972)011<0283:tlsmos>2.0.co;2

Demoz, B. B., Starr, D. O., Chan, K. R., & Bowen, S. W. (1998). Wavelet analysis of dynamical processes in cirrus. *Geophysical Research Letters*, *25*(9), 1347–1350. https://doi.org/10.1029/97gl03226

Esselborn, M., Wirth, M., Fix, A., Tesche, M., & Ehret, G. (2008). Airborne high spectral resolution lidar for measuring aerosol extinction and backscatter coefficients. *Applied Optics*, *47*, 346–358. https://doi.org/10.1364/AO.47.000346

Freudenthaler, V., Esselborn, M., Wiegner, M., Heese, B., Tesche, M., Ansmann, A., et al. (2009). Depolarization ratio profiling at several wavelengths in pure Saharan dust during SAMUM 2006. *Tellus B: Chemical and Physical Meteorology*, *61*, 165–179. https://doi.org/10.1111/j.1600-0889.2008.00396.x

Gasteiger, J., Groß, S., Sauer, D., Haarig, M., Ansmann, A., & Weinzierl, B. (2017). Particle settling and vertical mixing in the Saharan air layer as seen from an integrated model, lidar, and in situ perspective. *Atmospheric Chemistry and Physics*, *17*(1), 297–311. https://doi.org/10.5194/acp-17-297-2017

German Aerospace Center. (2016). https://doi.org/10.17616/R39Q0T
Groß, S., Freudenthaler, V., Schepanski, K., Toledano, C., Schäfler, A., Ansmann, A., & Weinzierl, B. (2015). Optical properties of long-range transported Saharan dust over Barbados as measured by dual-wavelength depolarization Raman lidar measurements. *Atmospheric Chemistry and Physics*, *15*, 11067–11080. https://doi.org/10.5194/acp-15-11067-2015
Groß, S., Wiegner, M., Freudenthaler, V., & Toledano, C. (2011). Lidar ratio of Saharan dust over Cape Verde islands: Assessment and error calculation. *Journal of Geophysical Research: Atmospheres*, *116*. https://doi.org/10.1029/2010JD015435
Gutleben, M., Groß, S., & Wirth, M. (2019). Cloud macro-physical properties in Saharan-dust-laden and dust-free North Atlantic trade wind regimes: A lidar case study. *Atmospheric Chemistry and Physics*, *19*(16), 10659–10673. https://doi.org/10.5194/acp-19-10659-2019
Gutleben, M., Groß, S., Wirth, M., Emnde, C., & Mayer, B. (2019). Impacts of water vapor on Saharan air layer radiative heating. *Geophysical Research Letters*, *46*(24), 14854–14862. https://doi.org/10.1029/2019GL085344
Gutleben, M., Groß, S., Wirth, M., & Mayer, B. (2020). Radiative effects of long-range-transported Saharan air layers as determined from airborne lidar measurements. *Atmospheric Chemistry and Physics*, *20*(20). https://doi.org/10.5194/acp-2020-420
Huneeus, N., Schulz, M., Balkanski, Y., Griesfeller, J., Prospero, J., Kinne, S., & Zender, C. S. (2011). Global dust model intercomparison in AeroCom phase I. *Atmospheric Chemistry and Physics*, *11*, 7781–7816. https://doi.org/10.5194/acp-11-7781-2011
Kiemle, C., Wirth, M., Fix, A., Ehret, G., Schumann, U., Gardiner, T., & Stiller, G. (2008). First airborne water vapor lidar measurements in the tropical upper troposphere and mid-latitudes lower stratosphere: Accuracy evaluation and intercomparisons with other instruments. *Atmospheric Chemistry and Physics*, *8*(17), 5245–5261. https://doi.org/10.5194/acp-8-5245-2008
Kolmogorov, A. (1941). The local structure of turbulence in incompressible viscous fluid for very large Reynolds' numbers. *Doklady Akademii Nauk SSSR*, *30*, 301–305
Konow, H., Jacob, M., Ament, F., Crewell, S., Ewald, F., Hagen, M., et al. (2018). *HALO microwave package measurements during next-generation remote sensing for validation studies 2 (NARVAL2)*. World Data Center for Climate (WDCC) at DKRZ. https://doi.org/10.1594/wdcc/halo_measurements_3
Krautstrunk, M., & Giez, A. (2012). The transition from FALCON to HALO era airborne atmospheric research. In U. Schumann (Ed.), *Atmospheric physics* (pp. 609–624). Springer Berlin Heidelberg. https://doi.org/10.1007/978-3-642-30183-4_37
Lilly, D. K. (1983). Stratified turbulence and the mesoscale variability of the atmosphere. *Journal of the Atmospheric Sciences*, *40*(3), 749–761.
Lomb, N. R. (1976). Least-squares frequency analysis of unequally spaced data. *Astrophysics and Space Science*, *39*(2), 447–462. https://doi.org/10.1007/bf00648343
Mahnke, P., Klingenberg, H., Fix, A., & Wirth, M. (2007). Dependency of injection seeding and spectral purity of a single resonant KTP optical parametric oscillator on the phase matching condition. *Applied Physics B*, *89*(1), 1–7. https://doi.org/10.1007/s00340-007-2746-z
Maring, H. (2003). Mineral dust aerosol size distribution change during atmospheric transport. *Journal of Geophysical Research: Atmospheres*, *108*(D19). https://doi.org/10.1029/2002jd002536
Messager, C., Parker, D. J., Reitebuch, O., Agusti-Panareda, A., Taylor, C. M., & Cuesta, J. (2009). Structure and dynamics of the Saharan atmospheric boundary layer during the West African monsoon onset: Observations and analyses from the research flights of 14 and 17 July 2006. *Quarterly Journal of the Royal Meteorological Society*, *136*(S1), 107–124. https://doi.org/10.1002/qj.469
Moulin, C., Lambert, C. E., Dulac, F., & Dayan, U. (1997). Control of atmospheric export of dust from North Africa by the North Atlantic oscillation. *Nature*, *387*(6634), 691–694. https://doi.org/10.1038/42679
Nicoll, K. A., Harrison, R. G., & Ulanowski, Z. (2010). Observations of Saharan dust layer electrification. *Environmental Research Letters*, *6*(1), 014001. https://doi.org/10.1088/1748-9326/6/1/014001
Prospero, J. M., & Carlson, T. N. (1972). Vertical and areal distribution of Saharan dust over the western equatorial North Atlantic Ocean. *Journal of Geophysical Research*, *77*, 5255–5265. https://doi.org/10.1029/JC077i027p05255
Prospero, J. M., & Lamb, P. J. (2003). African droughts and dust transport to the Caribbean: Climate change implications. *Science*, *302*, 1024–1027. https://doi.org/10.1126/science.1089915
Reichert, R., Kaifler, B., Kaifler, N., Rapp, M., Pautet, P.-D., Taylor, M. J., & Kivi, R. (2019). Retrieval of intrinsic mesospheric gravity wave parameters using lidar and airglow temperature and meteor radar wind data. *Atmospheric Measurement Techniques*, *12*(11), 5997–6015. https://doi.org/10.5194/amt-12-5997-2019
Reid, J. S. (2003). Analysis of measurements of Saharan dust by airborne and ground-based remote sensing methods during the Puerto Rico Dust Experiment (PRIDE). *Journal of Geophysical Research - D: Atmospheres*, *108*(D19). https://doi.org/10.1029/2002jd002493
Renard, J.-B., Dulac, F., Durand, P., Bourgeois, Q., Denjean, C., Vignelles, D., & Mallet, M. (2018). In situ measurements of desert dust particles above the western Mediterranean Sea with the balloon-borne Light Optical Aerosol Counter/sizer (LOAC) during the ChArMEx campaign of summer 2013. *Atmospheric Chemistry and Physics*, *18*(5), 3677–3699. https://doi.org/10.5194/acp-18-3677-2018
Scargle, J. D. (1982). Studies in astronomical time series analysis. II - Statistical aspects of spectral analysis of unevenly spaced data. *The Astrophysical Journal*, *263*, 835. https://doi.org/10.1086/160554
Stevens, B., Ament, F., Bony, S., Crewell, S., Ewald, F., Groß, S., & Zinner, T. (2019). A high-altitude long-range aircraft configured as a cloud observatory: The NARVAL expeditions. *Bulletin of the American Meteorological Society*, *100*. https://doi.org/10.1175/bams-d-18-0198.1
Sunnu, A., Afeti, G., & Resch, F. (2008). A long-term experimental study of the Saharan dust presence in West Africa. *Atmospheric Research*, *87*(1), 13–26. https://doi.org/10.1016/j.atmosres.2007.07.004
Taylor, G. I. (1935). Statistical theory of turbulence. *Proceedings of the Royal Society of London. Series A*, *151*(873), 421–444. https://doi.org/10.1098/rspa.1935.0158
Turner, J. (1973). *Buoyancy effects in fluids*. Cambridge England: University Press.
van der Does, M., Knippertz, P., Zschenderlein, P., Harrison, R. G., & Stuut, J.-B. W. (2018). The mysterious long-range transport of giant mineral dust particles. *Science Advances*, *4*(12), eaau2768. https://doi.org/10.1126/sciadv.aau2768
Wang, L., & Sassen, K. (2006). Cirrus mammatus properties derived from an extended remote sensing dataset. *Journal of the Atmospheric Sciences*, *63*(2), 712–725. https://doi.org/10.1175/jas3648.1
Wang, L., & Sassen, K. (2008). Wavelet analysis of cirrus multiscale structures from lidar backscattering: A cirrus uncinus complex case study. *The Journal of Applied Meteorology and Climatology*, *47*(10), 2645–2658. https://doi.org/10.1175/2008jamc1788.1
Weinzierl, B., Ansmann, A., Prospero, J. M., Althausen, D., Benker, N., Chouza, F., & Walser, A. (2017). The Saharan aerosol long-range transport and aerosol-cloud-interaction experiment: Overview and selected highlights. *Bulletin of the American Meteorological Society*, *98*, 1427–1451. https://doi.org/10.1175/BAMS-D-15-00142.1

Weinzierl, B., Sauer, D., Esselborn, M., Petzold, A., Veira, A., Rose, M., & Freudenthaler, V. (2011). Microphysical and optical properties of dust and tropical biomass burning aerosol layers in the Cape Verde region: An overview of the airborne in situ and lidar measurements during SAMUM-2. *Tellus B: Chemical and Physical Meteorology*, *63*(4), 589–618. https://doi.org/10.1111/j.1600-0889.2011.00566.x

Wirth, M., Fix, A., Mahnke, P., Schwarzer, H., Schrandt, F., & Ehret, G. (2009). The airborne multi-wavelength water vapor differential absorption lidar WALES: System design and performance. *Applied Physics B*, *96*, 201–213. https://doi.org/10.1007/s00340-009-3365-7